Computer Assisted Methods in Engineering and Science, **22**: 115–139, 2015.

Imperfection sensitivity of shear banding in gradient-dependent Cam-clay plasticity model

Anna Stankiewicz
Cracow University of Technology, Faculty of Civil Engineering
Institute for Computational Civil Engineering
Warszawska 24, 31-155 Cracow, Poland
e-mail: a.stankiewicz@L5.pk.edu.pl

The paper deals with the numerical simulation of strain localization in granular two-phase material. A gradient enhancement of modified Cam-clay model is introduced to overcome the problem of spurious discretization sensitivity of finite element solution. Two- and three-field finite elements implemented in the finite element analysis program (FEAP) are used in numerical simulations. The attention is focused on imperfection sensitivity of shear banding simulations. An application of the modelling framework to the slope stability problem is also included.

Keywords: two-phase medium, finite element method, plasticity, Cam-clay model, gradient regularization, localization, imperfection sensitivity.

1. Introduction

The material softening and the non-symmetry of the tangent stiffness operator are possible sources of strain localization in the form of shear banding encountered for instance in soil. Selected aspects of the numerical simulation of these phenomenon in granular materials are addressed in this paper. The problems such as a loss of material stability and the ill-posedness of governing equations of the boundary value problem resulting in a pathological mesh sensitivity of numerical results are first discussed. Different techniques used to overcome the problem of discretization sensitivity in the presence of strain localization are reviewed. The gradient-dependent Cam-clay plasticity model is applied to investigate the influence of imperfections on predicted shear banding patterns. Moreover, the cut slope stability benchmark is analyzed including the evolution of pore pressure, i.e. within the framework of two-phase modelling. The computations are carried out using two and three-field finite elements implemented in the FEAP package.

The issue of material instabilities causing strain localization was investigated for example in the review papers [13, 39, 66], in the extensive study of bifurcations in geomaterials [64] and in the proceedings of the International Union of Theoretical and Applied Mechanics (IUTAM) symposium [14]. Discussion of numerical finite element method (FEM) simulations of shear banding combined with experimental research can be found in [53]. If a material instability [26, 34] is encountered in the deformation history of a body, the strains often localize in a number of narrow bands, while the remaining parts of the body unload. Within a classical continuum formulation and for static problems this phenomenon is associated with a loss of ellipticity of the governing partial differential equations. Therefore, discretization methods used to solve these equations may yield mesh-sensitive and hence questionable results. To overcome this problem, a form of rate-dependent or non-local enhancement of the constitutive model should be adopted [13, 54]. The non-locality may have the form of micropolarity, integral averaging or spatial gradient-dependence. All these approaches imply the introduction of an internal length parameter in the continuum description.

In certain cases, for instance for the simulation of discrete fissures in rocks, discontinuum modelling can also be an option.

The developments of the last ten years concerning the problem of numerical simulations of localized deformation bands in multiphase (granular) media have been covered among others in [5, 7, 8, 10, 18, 25, 32, 41, 70, 71]. In [7] the problem of deformation and strain localization in partially saturated porous medium is considered and a constitutive model (extension of the modified Cam-clay model) for such a three-phase medium is proposed. A new, small-strain constitutive model of sand taking into account the essential features of granular materials is proposed in [18]. In [41] a general variational framework of Cam-clay theory is constructed within the finite deformation plasticity. The propagation of multiple shear zones in the interior of cohesionless sand is analyzed in [70]. The hypoplastic constitutive model enhanced by a characteristic length of micro-structure by means of the non-local theory has been applied in the finite element calculations. In [71] the issue of internal length scale introduced by the fluid-solid interaction is considered in a dynamic context. A strain localization phenomenon in 3D specimen of dense saturated sand under triaxial loading conditions is studied in [32]. The main focus in [32] is to investigate the role of the fluid components and the influence of factors such as permeability, water suction, draining conditions and geometry of the sample on formation and development of strain localization patterns. The problem of dispersive wave propagation in two-phase, fluid-saturated softening medium is addressed in [10]. The lack of regularization effect due to vanishing internal length scale is indicated. The stability issues in the presence of material softening and within gradient theories are examined in [5]. The paper by Gryczmański [25] is a review of the research on phenomena occurring in overconsolidated (and thus prone to softening and instabilities) soils at small strains. In [8] the effect of varying degree of saturation on shear band initiation in granular materials is investigated. The coupled solid deformation and fluid flow problem is solved using stabilized low-order mixed finite elements.

In this paper, the attention is focused on the Cam-clay model of cohesive soil and its performance. On one hand, this paper has an overview character. On the other hand, it is focused on examination of the role of imperfections in the analysis of the shear banding phenomenon. A practical application of the developed two-phase regularized soil model to the solution of a slope stability problem is also shown. The paper is a continuation of the studies reported in [55–57]. For completeness, the issue of ill-posedness of the boundary value problem and the main aspects of the regularized plastic flow theory as well as of granular material modelling are first recalled.

The paper is organized as follows. In Sec. 2 the sources of spurious discretization sensitivity of finite element solution in the presence of material instability and the approaches used to overcome the problem are briefly discussed. The adopted two-phase continuum theory for a granular material is described in Sec. 3. In Sec. 4, the gradient-enhanced Cam-clay plasticity model is presented and the formulation of an appropriate three-field finite element is presented in Sec. 5. The influence of imperfections is examined in Sec. 6 and the results of the numerical analysis of steep slope stability benchmark are included in Sec. 7. The computations are carried out using FEAP package. The paper ends with final remarks in Sec. 8.

2. Strain localization and regularization techniques

The sources of localization phenomena lie at the meso- or micro-level of observation (e.g. heterogeneity or local material defects). Following [44] the problem of material instabilities inducing a loss of ellipticity and strain localization is now recapitulated. A broader discussion of the issues can be found in [13, 39, 54, 66] and the study of bifurcations in geomaterials in [64]. The more general theoretical considerations are gathered in [46, 47].

The material stability [34, 36, 67] is determined by the condition of positive second-order work density

$$\dot{\epsilon}_{ij}\dot{\sigma}_{ij} > 0. \tag{1}$$

In the above inequality $\dot{\epsilon}_{ij}$ and $\dot{\sigma}_{ij}$ are the strain and stress rate tensors, respectively, and the summation convention is adopted. The consideration is limited to incrementally linear constitutive equations:

$$\dot{\sigma}_{ij} = D_{ijkl}\dot{\epsilon}_{kl}. \tag{2}$$

The loss of positive-definiteness of the tangent stiffness tensor D_{ijkl}, i.e. the singularity of the symmetric part of D_{ijkl} indicates the material instability:

$$\det(D_{ijkl} + D_{klij}) = 0. \tag{3}$$

When the material stability is lost (due to softening or nonsymmetry of the tangent operator) the so-called discontinuous bifurcation can occur, cf. [13, 40, 42, 48, 52, 67]. In such a case the continuity of the displacement field and the equilibrium condition are preserved at each point, while the jump of strain is permitted across a discontinuity surface with normal ν_i, see Fig. 1

$$[\![u_{i,j}]\!] \equiv u^{+}_{i,j} - u^{-}_{i,j} \neq 0, \tag{4}$$

where $[\![\ \ ]\!]$ denotes a jump of a quantity while the '+' and '−' signs refer to the two sides of the discontinuity surface. In order to satisfy the kinematic compatibility condition the strain rate jump across discontinuity surface has to be expressed as

$$[\![\dot{\epsilon}_{ij}]\!] = \frac{1}{2}(\nu_i\mu_j + \nu_j\mu_i), \tag{5}$$

where μ_i is an arbitrary vector. Using the linear constitutive Eq. (2), the stress rate jump is obtained at the onset of the discontinuity

$$[\![\dot{\sigma}_{ij}]\!] = D_{ijkl}[\![\dot{\epsilon}_{kl}]\!], \tag{6}$$

where it is assumed that the same tangent stiffness moduli represent the material behaviour on both sides of the discontinuity surface.

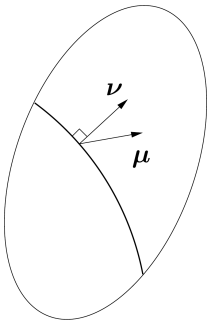

Fig. 1. Material instability: 2D idealization of discontinuity surface and vectors $\boldsymbol{\nu}$ (normal) and $\boldsymbol{\mu}$ (defining instability mode).

In [16] different modes of the localized bifurcation in elastoplastic solids are distinguished. The authors describe plastic/plastic and elastic/plastic bifurcation modes.

From the equilibrium condition the zero value of the jump of traction rate across the discontinuity plane results in:

$$[\![\dot{t}_j\ ]\!] = \nu_i[\![\dot{\sigma}_{ij}\ ]\!] = 0. \tag{7}$$

Now, substituting Eq. (6) and Eq. (5) into Eq. (7), and using the symmetry property $D_{ijkl} = D_{ijlk}$ the following equation is obtained:

$$(\nu_i D_{ijkl}\nu_l)\mu_k = 0. \tag{8}$$

It has a non-trivial solution only when the determinant of the so-called acoustic tensor (product within brackets) vanishes:

$$\det(Q_{jk}) = 0. \tag{9}$$

The singularity of the acoustic tensor implies a local loss of ellipticity of the rate equilibrium equations and thus the ill-posedness of the boundary value problem (BVP). Thereby, the strain localization (e.g. shear band formation) is initiated. A shear band can be defined as a zone of intense deformation bounded by two discontinuity surfaces. For a classical material model, the distance between these two surfaces remains undefined which results in their coincidence and localization in a set of measure zero. In this paper the notion of strain localization is understood in a broader sense, as the emergence of bands of concentrated deformation caused by material instabilities. Nevertheless, the first point in the deformation history for which the acoustic tensor becomes singular marks the possible onset of localization.

It should be mentioned that in addition to the so-called weak discontinuities (discontinuities of strain field) also strong discontinuities (jumps in the displacement field) can be considered, cf. [68]. For such a case a displacement discontinuity (crack) occurs along surface interfaces while in the other parts of the body ellipticity and thus well-posedness of BVP are preserved. In computations using numerical methods (e.g., FEM) in the presence of the weak discontinuities the results become pathologically dependent on discretization density (and the mesh alignment). The problem results from the attempts to simulate the localization in the smallest material volume admitted by the adopted discretization. An example of mesh-dependent numerical results is presented in Fig. 2 for a plane strain biaxial compression test (which will further be discussed in Sec. 6) and the classical Cam-clay plasticity model.

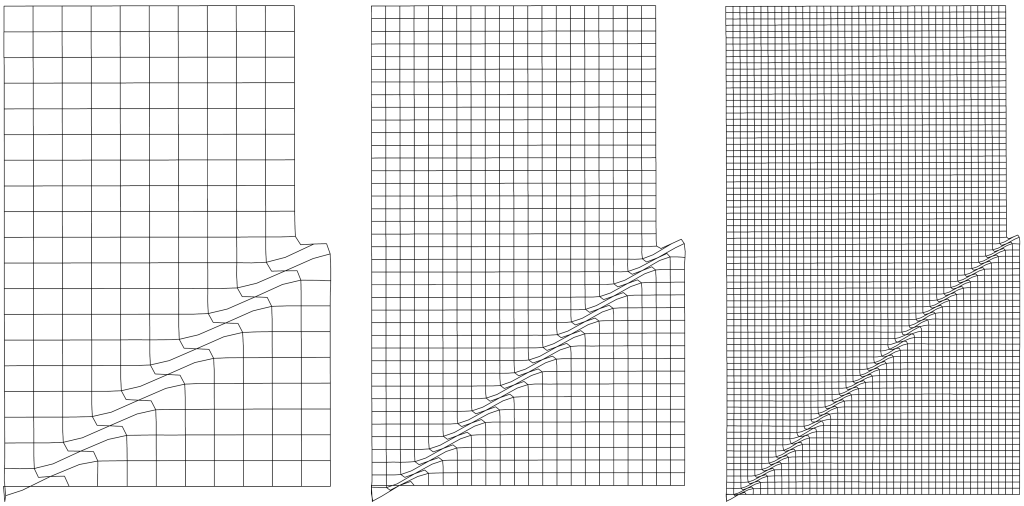

Fig. 2. Scaled incremental displacements for local model in biaxial compression test.

Two different approaches are applied to overcome the problem. One possibility is to permit the occurrence of strong discontinuity surfaces or lines. This approach is recommended for instance for a quasi-brittle materials which undergo macroscoping cracking. The concentrated deformation is then modelled using interface finite elements (see, e.g., [51]) or the extended finite element method (XFEM) resulting from the use of partition of unity (see, e.g., [3, 17, 35, 65]). In this method the approximation basis of the finite elements used to simulate the formation and propagation of strong discontinuities through element domains are enriched with Heaviside-type functions.

The problem of ill-posedness of the mathematical model can also be solved by application of enhanced (regularized) continuum theories. In this concept higher order deformation gradients or time rates are introduced into the constitutive description. The spurious mesh sensitivity of

the numerical simulation results is then removed by incorporating the so-called internal length scale which defines a (non-zero) width of the localization band and is understood as an additional material parameter. In granular materials, the internal length parameter is related to the average grain diameter: directly in micropolar models [59, 60] or indirectly in nonlocal ones [70].

The regularized models include the plastic flow theories which incorporate higher deformation gradients, see, e.g., [1, 11, 15, 30, 37, 43, 58, 63], and gradient theories of continuum damage, e.g., [2, 19, 29, 31, 45]. An alternative solution is provided by a micropolar continuum, e.g., [9, 38, 61], rate dependent models, in particular viscoplastic, see for instance [21, 33, 54, 69], or nonlocal integral models, see, e.g., [4, 6, 23, 28, 49].

3. Numerical modelling of granular material

In Fig. 3 the porous and granular nature of soil is depicted. Soil is a multiphase material which consists of a skeleton and voids filled with fluids. In the case of partially saturated soil voids are partly occupied by water and partly by air. Such a three-phase medium is described by: the solid displacement, water pore pressure and air pore pressure. When pores are completely filled with water then soil is fully saturated and it is modelled as a two-phase medium. The problem variables are: the solid displacement vector and the water pore pressure. Noteworthy are two limiting cases of the so-called drained state and undrained state. In the former case, if long-term load together with appreciable permeability is assumed, the fluid flows out freely and the pore pressure does not depend on the material deformation. Thus, the excess pore pressure p_f is equal to zero and soil can be treated as a one-phase medium. In the latter case of undrained state, for rapidly loaded soil with low (zero) permeability, the fluid motion relative to soil skeleton is negligible. The consideration can then also be limited to a one-phase medium.

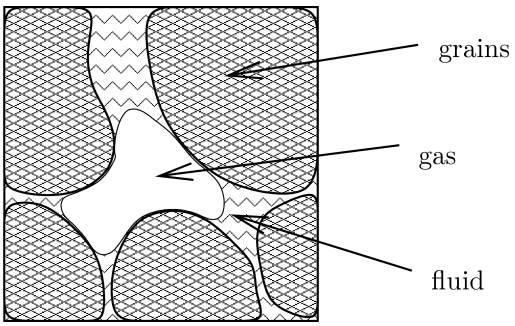

Fig. 3. Soil as a multiphase, porous and granular medium.

The case of partially saturated soil is not investigated in the present paper. The attention is focused on fully saturated material. The common assumption of solid grains incompressibility is adopted. The behaviour of a two-phase medium is governed by the momentum and mass balance equations [62, 72]:

$$\boldsymbol{L}^{\mathrm{T}}\boldsymbol{\sigma}_t + \widehat{\rho}\boldsymbol{g} = \boldsymbol{0}, \tag{10}$$

$$\nabla^{\mathrm{T}}\dot{\boldsymbol{u}} + \nabla^{\mathrm{T}}\boldsymbol{v}_d + n\frac{\dot{p}_f}{K_f} = 0. \tag{11}$$

The balance of the medium is maintained by the total stress $\boldsymbol{\sigma}_t$ which decomposes into the effective stress $\boldsymbol{\sigma}$ in the soil skeleton and the (excess) pore pressure p_f in the fluid constituents. The adopted sign convention is that the compressive pressure is regarded as positive

$$\boldsymbol{\sigma_t} = \boldsymbol{\sigma} - \boldsymbol{\Pi}p_f. \tag{12}$$

This decomposition is necessary to reproduce the dominant role of the solid phase in the load-carrying capacity of soil. The effective stress is responsible for the deformation and limit states of saturated soil and appears in the constitutive equations. The saturated density of the solid-fluid mixture is given by

$$\widehat{\rho} = (1-n)\rho_s + n\rho_f, \tag{13}$$

where ρ_s is the density of the solid phase and ρ_f denotes the density of the fluid phase. The porosity n and the void ratio e are related by

$$n = \frac{e}{1+e}, \qquad e = \frac{V_p}{V_s}, \tag{14}$$

where V_p is the pore volume and V_s is the skeleton volume.

The fluid flow velocity is denoted by $\boldsymbol{v}_d$ and assumed to follow Darcy's law (gravity term is neglected here):

$$\boldsymbol{v}_d = -\boldsymbol{k}\nabla\frac{p_f}{\gamma_f}. \tag{15}$$

Moreover, $\boldsymbol{L}$ is a differential operator matrix (Voigt's matrix-vector notation is used), $\boldsymbol{g}$ is the gravitation vector, $\boldsymbol{u}$ is the displacement vector and $\dot{\boldsymbol{u}}$ denotes its first time derivative, K_f is the bulk modulus of the fluid, $\boldsymbol{k}$ is the permeability matrix (with the assumption of isotropy it is substituted by a scalar quantity), and finally superscript T is the transpose symbol.

The governing (differential) Eqs. (10) and (11) require appropriate boundary and initial conditions. The initial conditions for the displacements and pore pressures at time $t = 0$ are:

$$\begin{aligned} &\boldsymbol{u} = \boldsymbol{u}_0, \\ &p_f = p_{f0}. \end{aligned} \tag{16}$$

The boundary conditions to be satisfied at any time t are:

$$\begin{aligned} &\boldsymbol{\sigma}_t\boldsymbol{\nu} = \widehat{\boldsymbol{t}} \quad \text{on} \quad \Gamma_t, \\ &\boldsymbol{v}_d\boldsymbol{\nu} = \widehat{\boldsymbol{q}} \quad \text{on} \quad \Gamma_q, \\ &\boldsymbol{u} = \widehat{\boldsymbol{u}} \quad \text{on} \quad \Gamma_u, \\ &p_f = \widehat{p}_f \quad \text{on} \quad \Gamma_p, \end{aligned} \tag{17}$$

where $\Gamma_t \cdots \Gamma_p$ are appropriate boundary parts, such that $\Gamma_t \cap \Gamma_u = \varnothing$, $\Gamma_t \cup \Gamma_u = \Gamma$, $\Gamma_q \cap \Gamma_p = \varnothing$, $\Gamma_q \cup \Gamma_p = \Gamma$.

The complex microstructure of soil determines its features and causes instabilities observed at macroscopic scale. One of the fundamental soil features is its sensitivity to volume changes. They can be caused either by a change in effective confining pressure or by a rearrangement of grains in the structure due to shearing load. This is conveniently modelled by a suitable plastic flow theory. The tendency to reach a critical state, in which only the deviatoric plastic strain increments are observed and the strength and volume are constant should also be taken into account in material modelling. Therefore, the modified Cam-clay model originally proposed in [50], belonging to the critical state models [20], has been chosen to describe the behaviour of the soil skeleton and is summarized next.

4. Regularized cam-clay model

The yield function for the modified Cam-clay model, see Fig. 4, can be written as

$$f = q^2 + M^2 p(p - p_c) = 0, \tag{18}$$

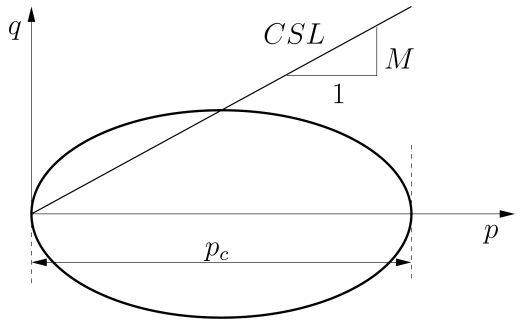

Fig. 4. Material model: yield surface. CSL denotes the critical state line.

where the equivalent deviatoric stress q is defined as $q = \sqrt{3J_2}$, M is a function of the internal friction angle ϕ, $M = \dfrac{6\sin\phi}{3-\sin\phi}$, p is the effective pressure acting on the soil skeleton, which is assumed to evolve according to the following secant relation [24]:

$$p(\Delta\theta^{\mathrm{e}}) = p_0 \exp\left[-\frac{1+e_0}{\kappa}\Delta\theta^{\mathrm{e}}\right], \tag{19}$$

where e_0 denotes the initial void ratio, κ is the swelling index which defines the inclination of the unloading and reloading diagram relating the void ratio to $\ln(p)$, θ^{e} is the volumetric part of the elastic strain tensor. Further more, p_c is the current preconsolidation pressure, the evolution of which is given by the formula similar to Eq. (19):

$$p_c(\Delta\theta^{\mathrm{p}}) = p_{c0} \exp\left[-\frac{1+e_0}{\lambda-\kappa}\Delta\theta^{\mathrm{p}}\right], \tag{20}$$

where λ is the inclination of the virgin consolidation line in 1+e vs $\ln(p)$ diagram, θ^{p} is the volumetric part of the plastic strain tensor. Since the fraction $\frac{1+e_0}{\lambda-\kappa}$ is positive, the signs of $\dot{p_c}$ and $\dot{\theta^p}$ must be opposite. This means that the hardening (contraction) is observed for decreasing increment of plastic volumetric strain ($\dot{\theta^p} < 0 \Longrightarrow \dot{p_c} > 0$). The material exhibits softening (dilatation) for increasing increment of plastic volumetric strain ($\dot{\theta^p} > 0 \Longrightarrow \dot{p_c} < 0$). Note that the hardening rule has the character of the mixed hardening. Let us introduce the so-called over-consolidation ratio (OCR) which is a relation between the initial preconsolidation pressure p_{c0} and the initial compressive pressure:

$$OCR = -\frac{p_{c0}}{p_0}. \tag{21}$$

If $OCR \gg 1$ the soil is overconsolidated and has a tendency to dilatant (softening) behaviour. The soil for which $OCR = 1$ is called normally consolidated and it exhibits contraction (hardening).

As stated in Sec. 2, in order to avoid the loss of ellipticity of the governing equations and to stabilize the numerical response in the presence of material instabilities the regularization of the Cam-clay model is necessary. The Cam-clay yield function is made dependent on the Laplacian of the plastic multiplier Λ and takes the following form [55–57]:

$$F = q^2 + M^2 p\,[p - p_c(\theta^{\mathrm{p}}) + g\nabla^2(\Lambda)], \tag{22}$$

where $g > 0$ is a gradient scaling factor proportional to a square of an internal length scale l. The yield (and plastic consistency) condition is thus a differential equation to be solved in parallel with the standard governing equations. The yield condition $F = 0$ is recast into a weak format and the plastic multiplier is discretized in the monolithic solution algorithm.

5. Three-field finite element

The governing equations in the analysis of the coupled deformation and fluid flow problem combined with the gradient-enhanced plasticity modelling of the solid skeleton are derived from the mechanical equilibrium of the soil skeleton, the mass balance of the pore fluid and plastic consistency condition. The unknown variables in the obtained system of equations are not only the solid displacements, fluid pore pressure and plastic multiplier but also the displacement and pore pressure rates. The solution to such a system of equations requires the application of a stable and accurate time integration scheme. The discretization in time is usually carried out using the generalized trapezoidal method (called Θ-method). With this method, all time dependent variables are estimated at some intermediate point within the interval, depending on the chosen value of Θ. To assure the unconditional stability of the algorithm, the integration coefficient should satisfy the condition $\Theta \geq \frac{1}{2}$. This method and the problems of convergence, consistency and stability of the numerical algorithms (and various aspects of their analysis) are covered for instance in [27]. In the discussed implementation the backward Euler scheme with $\Theta = 1$ is used. The application of this integration method gives:

$$\boldsymbol{u}_{N+1} = \boldsymbol{u}_N + \Delta t \dot{\boldsymbol{u}}_{N+1}, \tag{23}$$

$$p_{N+1} = p_N + \Delta t \dot{p}_{N+1}. \tag{24}$$

To formulate a three-field $\boldsymbol{u} - p - \Lambda$ finite element the weak forms of Eqs. (10), (11) and (22) are required. The momentum balance equation in a weak form reads

$$\int_\Omega \boldsymbol{v}^{\mathrm{T}} (\boldsymbol{L}^{\mathrm{T}} \boldsymbol{\sigma}_t + \widehat{\rho} \boldsymbol{g}) \mathrm{d}\Omega = \boldsymbol{0}. \tag{25}$$

The mass balance equation is written as

$$\int_\Omega w \left(\nabla^{\mathrm{T}} \dot{\boldsymbol{u}} + \nabla^{\mathrm{T}} \boldsymbol{v}_d + n \frac{\dot{p}_f}{K_f} \right) \mathrm{d}\Omega = 0. \tag{26}$$

The weak form of the yield condition is

$$\int_\Omega v_p \, F(\boldsymbol{\sigma}, \Lambda, \nabla^2 \Lambda) \mathrm{d}\Omega = 0. \tag{27}$$

For the gradient-dependent yield function, i.e., for the plastic multiplier field homogeneous natural boundary conditions are postulated, cf. [12, 43]. In Eqs. (25)–(27) $\boldsymbol{v}$, w and v_p are suitable weighting functions. Integration of momentum and mass balance equations by parts and incorporation of natural boundary conditions lead to:

$$\int_\Omega (\boldsymbol{L}\boldsymbol{v})^{\mathrm{T}} \boldsymbol{\sigma}_t \mathrm{d}\Omega - \int_\Omega \boldsymbol{v}^{\mathrm{T}} \widehat{\rho} \boldsymbol{g} \mathrm{d}\Omega - \int_{\Gamma_t} \boldsymbol{v}^{\mathrm{T}} \widehat{\boldsymbol{t}} \mathrm{d}\Gamma = \boldsymbol{0}, \tag{28}$$

$$\int_\Omega w \nabla^{\mathrm{T}} \dot{\boldsymbol{u}} \, \mathrm{d}\Omega - \int_\Omega (\nabla w)^{\mathrm{T}} \boldsymbol{v}_d \, \mathrm{d}\Omega + \int_\Omega w \frac{n}{K_f} \dot{p}_f \, \mathrm{d}\Omega + \int_{\Gamma_q} w \, \widehat{\boldsymbol{q}} \mathrm{d}\Gamma = 0. \tag{29}$$

The backward Euler integration of Eqs. (28) and (29) over time increment Δt is performed and both Darcy's law and Terzaghi's decomposition of the total stress are introduced. The following finite element discretizations for displacements $\boldsymbol{u}$, excess pore pressure p_f and plastic multiplier Λ are introduced:

$$\boldsymbol{u} = \boldsymbol{N} \check{\boldsymbol{u}}, \qquad p_f = \boldsymbol{N}_p \check{\boldsymbol{p}}, \qquad \Lambda = \boldsymbol{h} \check{\boldsymbol{\Lambda}}, \tag{30}$$

where $\boldsymbol{N}$, $\boldsymbol{N}_p$ and $\boldsymbol{h}$ contain the respective interpolation polynomials and $\check{\boldsymbol{u}}$, $\check{\boldsymbol{\Lambda}}$ and $\check{\boldsymbol{p}}$ are vectors with the discrete nodal values. The weighting functions are interpolated similarly according to the Bubnov-Galerkin approach. In order to provide a proper balance between interpolations in this coupled problem [62, 72] the functions used to interpolate the unknown fields are quadratic for the displacements, linear for the pore pressure and cubic (Hermitean) for the plastic multiplier. In Fig. 5, the nodes with nodal degrees of freedom are shown. The displacements are interpolated between eight nodes while the excess pore pressure and the plastic multiplier between four nodes.

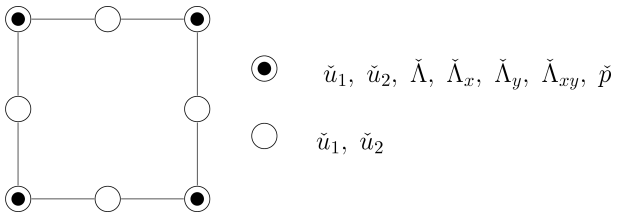

Fig. 5. Three-field u-p-Λ finite element.

The incremental-iterative algorithm with the following decomposition is used to linearize the governing equations at the current time instant:

$$\Delta\boldsymbol{\sigma}^{(i+1)} = \Delta\boldsymbol{\sigma}^{(i)} + \mathrm{d}\boldsymbol{\sigma}^{(i+1)}, \qquad \Delta p^{(i+1)} = \Delta p^{(i)} + \mathrm{d}p^{(i+1)}, \qquad \Delta\Lambda^{(i+1)} = \Delta\Lambda^{(i)} + \mathrm{d}\Lambda^{(i+1)}. \tag{31}$$

In Eqs. (31) $\mathrm{d}\boldsymbol{\sigma}$, $\mathrm{d}p$ and $\mathrm{d}\Lambda$ denote the corrections of increments computed in the current iteration $(i+1)$. The yield function F is developed in a truncated Taylor series around $(\boldsymbol{\sigma}^{(i)}, \Lambda^{(i)}, \nabla^2\Lambda^{(i)})$ to obtain the following incremental equation:

$$\int_\Omega v_p \left[\frac{\partial F}{\partial\boldsymbol{\sigma}}\mathrm{d}\boldsymbol{\sigma} + \frac{\partial F}{\partial\Lambda}\mathrm{d}\Lambda + \frac{\partial F}{\partial\nabla^2\Lambda}\nabla^2(\mathrm{d}\Lambda)\right]\mathrm{d}\Omega = -\int_\Omega v_p F\left(\boldsymbol{\sigma}^{(i)}, \Lambda^{(i)}, \nabla^2\Lambda^{(i)}\right)\mathrm{d}\Omega. \tag{32}$$

We eventually obtain the set of equations:

$$\begin{aligned}
&\int_\Omega \boldsymbol{B}^{\mathrm{T}}\frac{\mathrm{d}\boldsymbol{\sigma}}{\mathrm{d}\boldsymbol{\epsilon}}^{(i)}\boldsymbol{B}\mathrm{d}\Omega\Delta\check{\boldsymbol{u}}^{(i+1)} - \int_\Omega \boldsymbol{B}^{\mathrm{T}}\boldsymbol{\Pi}\boldsymbol{N}_p\mathrm{d}\Omega\Delta\check{\boldsymbol{p}}^{(i+1)} - \int_\Omega \boldsymbol{B}^{\mathrm{T}}\frac{\mathrm{d}\boldsymbol{\sigma}}{\mathrm{d}\Lambda}\boldsymbol{h}\mathrm{d}\Omega\Delta\check{\boldsymbol{\Lambda}}^{(i+1)} \\
&\qquad = \int_\Omega \boldsymbol{N}^{\mathrm{T}}\widehat{\rho}\boldsymbol{g}\mathrm{d}\Omega + \int_{\Gamma_t}\boldsymbol{N}^{\mathrm{T}}\widehat{\boldsymbol{t}}\mathrm{d}\Gamma - \int_\Omega\left(\boldsymbol{B}^{\mathrm{T}}\boldsymbol{\sigma}^{(i)} - \boldsymbol{B}^{\mathrm{T}}\boldsymbol{\Pi}p_f{}^{(i)}\right)\mathrm{d}\Omega, \\
&\int_\Omega \boldsymbol{N}_p^{\mathrm{T}}\boldsymbol{\Pi}^{\mathrm{T}}\boldsymbol{B}\mathrm{d}\Omega\Delta\check{\boldsymbol{u}}^{(i+1)} + \left(\frac{\Delta t}{\gamma_f}\int_\Omega(\nabla\boldsymbol{N}_p)^{\mathrm{T}}\boldsymbol{k}\nabla\boldsymbol{N}_p\mathrm{d}\Omega + \int_\Omega \boldsymbol{N}_p^{\mathrm{T}}\frac{n}{K_f}\boldsymbol{N}_p\mathrm{d}\Omega\right)\Delta\check{\boldsymbol{p}}^{(i+1)} \\
&= \Delta t\left(-\int_{\Gamma_q}\boldsymbol{N}_p{}^{\mathrm{T}}\widehat{\boldsymbol{q}}\mathrm{d}\Gamma - \int_\Omega \boldsymbol{N}_p^{\mathrm{T}}\boldsymbol{\Pi}^{\mathrm{T}}\boldsymbol{B}\mathrm{d}\Omega\dot{\check{\boldsymbol{u}}}^{(i)} - \frac{1}{\gamma_f}\int_\Omega(\nabla\boldsymbol{N}_p)^{\mathrm{T}}\boldsymbol{k}\nabla\boldsymbol{N}_p\mathrm{d}\Omega\check{\boldsymbol{p}}^{(i)} - \int_\Omega \boldsymbol{N}_p^{\mathrm{T}}\frac{n}{K_f}\boldsymbol{N}_p\mathrm{d}\Omega\dot{\check{\boldsymbol{p}}}^{(i)}\right), \\
&-\int_\Omega \boldsymbol{h}^{\mathrm{T}}\frac{\partial F}{\partial\boldsymbol{\sigma}}\frac{\mathrm{d}\boldsymbol{\sigma}}{\mathrm{d}\boldsymbol{\epsilon}}\boldsymbol{B}\mathrm{d}\Omega\Delta\check{\boldsymbol{u}}^{(i+1)} - \int_\Omega\left(\frac{\partial F}{\partial\boldsymbol{\sigma}}\frac{\mathrm{d}\boldsymbol{\sigma}}{\mathrm{d}\Lambda} + \frac{\partial F}{\partial\Lambda}\right)\boldsymbol{h}^{\mathrm{T}}\boldsymbol{h}\mathrm{d}\Omega\Delta\check{\boldsymbol{\Lambda}}^{(i+1)} - \int_\Omega \frac{\partial F}{\partial\nabla^2\Lambda}\boldsymbol{h}^{\mathrm{T}}\boldsymbol{s}\mathrm{d}\Omega\Delta\check{\boldsymbol{\Lambda}}^{(i+1)} \\
&\qquad = \int_\Omega \boldsymbol{h}F(\boldsymbol{\sigma}^{(i)}, \Lambda^{(i)}, \nabla^2\Lambda^{(i)})\mathrm{d}\Omega,
\end{aligned} \tag{33}$$

where the notations $\boldsymbol{B} = \boldsymbol{L}\boldsymbol{N}$ and $\boldsymbol{s} = \nabla^2\boldsymbol{h}$ are used. Moreover, $\dfrac{\mathrm{d}\boldsymbol{\sigma}}{\mathrm{d}\boldsymbol{\epsilon}}$ denotes the consistent tangent operator for the material model.

The obtained coupled system of linearized equations is now rewritten in a matrix form:

$$\begin{bmatrix} \boldsymbol{K}_{uu} & -\boldsymbol{K}_{up} & \boldsymbol{K}_{u\Lambda} \\ -\boldsymbol{K}_{up}^{\mathrm{T}} & \boldsymbol{K}_{pp} & \boldsymbol{0} \\ \boldsymbol{K}_{\Lambda u} & \boldsymbol{0} & \boldsymbol{K}_{\Lambda\Lambda} \end{bmatrix} \begin{bmatrix} \Delta\check{\boldsymbol{u}} \\ \Delta\check{\boldsymbol{p}} \\ \Delta\check{\boldsymbol{\Lambda}} \end{bmatrix} = \begin{bmatrix} \boldsymbol{f}_{\mathrm{ext}} - \boldsymbol{f}_{\mathrm{int}} \\ \boldsymbol{f}_f \\ \boldsymbol{f}_\Lambda \end{bmatrix}, \tag{34}$$

where the submatrices are defined as follows (the iteration index has been skipped):

$$\begin{aligned}
\boldsymbol{K}_{uu} &= \int_\Omega \boldsymbol{B}^{\mathrm{T}} \frac{\mathrm{d}\boldsymbol{\sigma}}{\mathrm{d}\boldsymbol{\epsilon}} \boldsymbol{B}\mathrm{d}\Omega, \\
\boldsymbol{K}_{u\Lambda} &= -\int_\Omega \boldsymbol{B}^{\mathrm{T}} \frac{\mathrm{d}\boldsymbol{\sigma}}{\mathrm{d}\Lambda} \boldsymbol{h}\mathrm{d}\Omega, \\
\boldsymbol{K}_{\Lambda u} &= -\int_\Omega \boldsymbol{h}^{\mathrm{T}} \frac{\partial F}{\partial \boldsymbol{\sigma}} \frac{\mathrm{d}\boldsymbol{\sigma}}{\mathrm{d}\boldsymbol{\epsilon}} \boldsymbol{B}\mathrm{d}\Omega, \\
\boldsymbol{K}_{\Lambda\Lambda} &= -\int_\Omega \left[\left(\frac{\partial F}{\partial \boldsymbol{\sigma}} \frac{\mathrm{d}\boldsymbol{\sigma}}{\mathrm{d}\Lambda} + \frac{\partial F}{\partial \Lambda} \right) \boldsymbol{h}^{\mathrm{T}}\boldsymbol{h} + g\boldsymbol{h}^{\mathrm{T}}\boldsymbol{s} \right] \mathrm{d}\Omega, \\
\boldsymbol{K}_{up} &= \int_\Omega \boldsymbol{B}^{\mathrm{T}} \boldsymbol{\Pi} \boldsymbol{N}_p \mathrm{d}\Omega, \\
\boldsymbol{K}_{pp} &= -\frac{\Delta t}{\gamma_f} \boldsymbol{H} - \boldsymbol{M}, \\
\boldsymbol{H} &= \int_\Omega (\nabla \boldsymbol{N}_p)^{\mathrm{T}} \boldsymbol{k} \nabla \boldsymbol{N}_p, \mathrm{d}\Omega, \\
\boldsymbol{M} &= \int_\Omega \boldsymbol{N}_p^{\mathrm{T}} \frac{n}{K_f} \boldsymbol{N}_p \mathrm{d}\Omega, \\
\boldsymbol{f}_{\mathrm{ext}} &= \int_\Omega \boldsymbol{N}^{\mathrm{T}} \widehat{\rho}\boldsymbol{g}\, \mathrm{d}\Omega + \int_{\Gamma_t} \boldsymbol{N}^{\mathrm{T}} \widehat{\boldsymbol{t}} \mathrm{d}\Gamma, \\
\boldsymbol{f}_{\mathrm{int}} &= \int_\Omega \left(\boldsymbol{B}^{\mathrm{T}}\boldsymbol{\sigma} - \boldsymbol{B}^{\mathrm{T}}\boldsymbol{\Pi} p_f \right) \mathrm{d}\Omega, \\
\boldsymbol{f}_f &= \Delta t \left(\int_{\Gamma_q} \boldsymbol{N}_p^{\mathrm{T}} \widehat{\boldsymbol{q}}\, \mathrm{d}\Gamma + \boldsymbol{K}_{up}^{\mathrm{T}} \check{\boldsymbol{u}} + \frac{1}{\gamma_f} \boldsymbol{H}\check{\boldsymbol{p}} + \boldsymbol{M}\check{\boldsymbol{p}} \right), \\
\boldsymbol{f}_\Lambda &= \int_\Omega \boldsymbol{h}^{\mathrm{T}} F(\boldsymbol{\sigma}, \Lambda, \nabla^2\Lambda) \mathrm{d}\Omega.
\end{aligned} \tag{35}$$

It should be noted that the tangent operator in Eq. (35) is nonsymmetric. If the gradient's influence is neglected, the two-phase Cam-clay plasticity model can be reduced to the classical

format, i.e., the plastic multiplier is not discretized and the first two rows of the set of equations are solved with $\boldsymbol{K}_{u\Lambda} = \boldsymbol{0}$. On the other hand, if the influence of the pore fluid changes is not taken into account an alternative two field problem of gradient plasticity is obtained with just the first and third fields to be determined.

6. Influence of imperfections

In order to examine the role of imperfections in the analysis of the shear banding localization phenomenon the biaxial compression test of drained soil sample (one-phase soil model described by the first and the third equation of system (34)) is considered. The size of the specimen is 1×2 m. It is discretized with 20×40 two-field gradient plasticity finite elements. In the computations the following material data are adopted: Poisson's ratio $\nu = 0.2$, swelling index $\kappa = 0.013$, initial void ratio $e_0 = 1.0$, hardening parameter $p_{c0} = 2.0$ MPa, compression index $\lambda = 0.032$, material constant $M = 1.1$. The initial stresses $\boldsymbol{\sigma}_0 = [-0.2, -0.2, -0.08, 0.0]$ MPa (necessary to start calculations when the Cam-clay model is used) are introduced by uniform compression. To load the sample a vertical traction downwards on the top edge is prescribed.

Unlike in dynamics (cf. [22]), in static simulations of localization phenomena the imperfections merely trigger the process and set the initial position of deformation bands. Here, the analysis is focused on the influence of imperfection location, size and intensity on the results. In Fig. 6 the locations of the imperfection area are shown. The following five cases are considered:

- case A – 10% four-element imperfection located in the middle of the sample,
- case B – 10% four-element imperfection located in the middle of the left edge of the sample,
- case C – 1% four-element imperfection located in the middle of the left edge of the sample,
- case D – 10% sixteen-element imperfection located in the middle of the left edge of the sample,
- case E – two 10% four-element imperfections located in the left edge of the sample.

In the presented tests, four or eight elements are assigned the 10% or 1% smaller value of the initial overconsolidation measure. However, the different values of the initial void ratio can also be used in order to start the localization process.

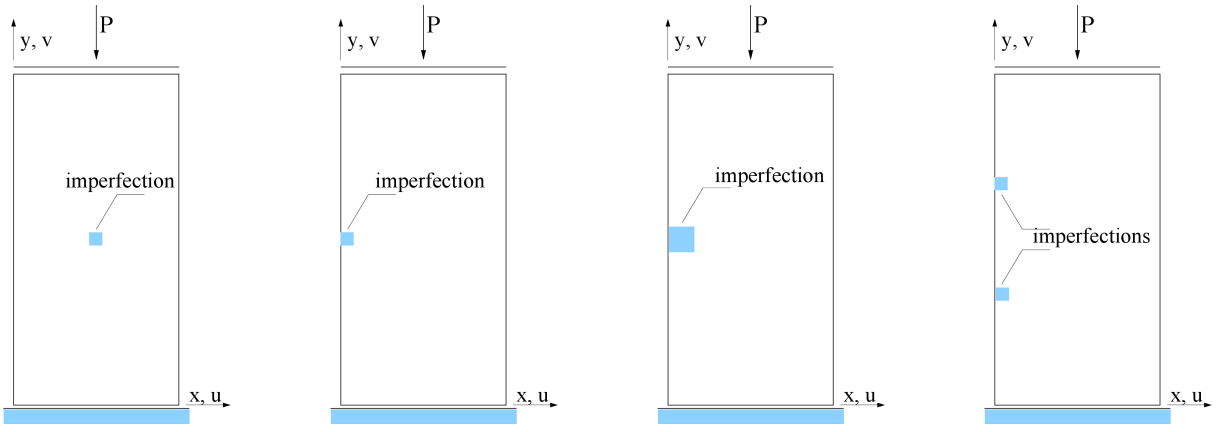

Fig. 6. Imperfection location.

The load-displacement curves for cases A–E are shown in Fig. 7. The diagrams almost coincide with each other (only the solution for case D exhibits lower load-carrying capacity due to larger imperfect area). In Figs. 8–12 the contour plots with the distributions of invariant J_2^{ϵ} of the strain

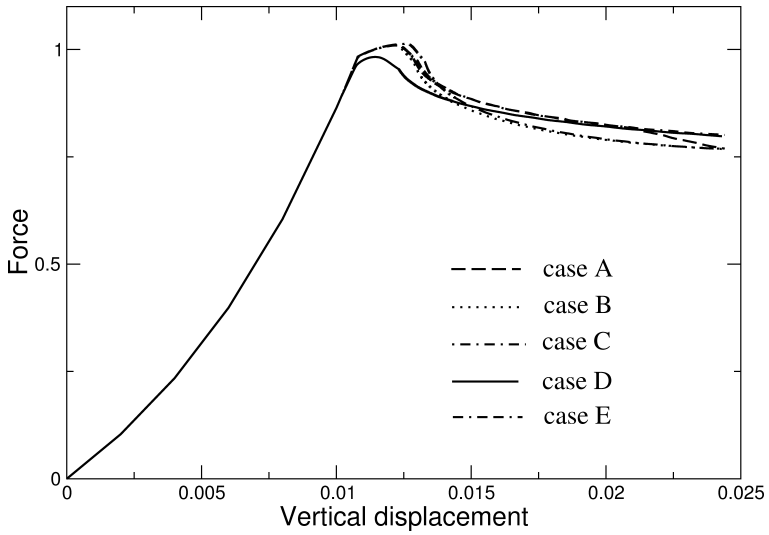

Fig. 7. Load-deformation curves for cases A–E.

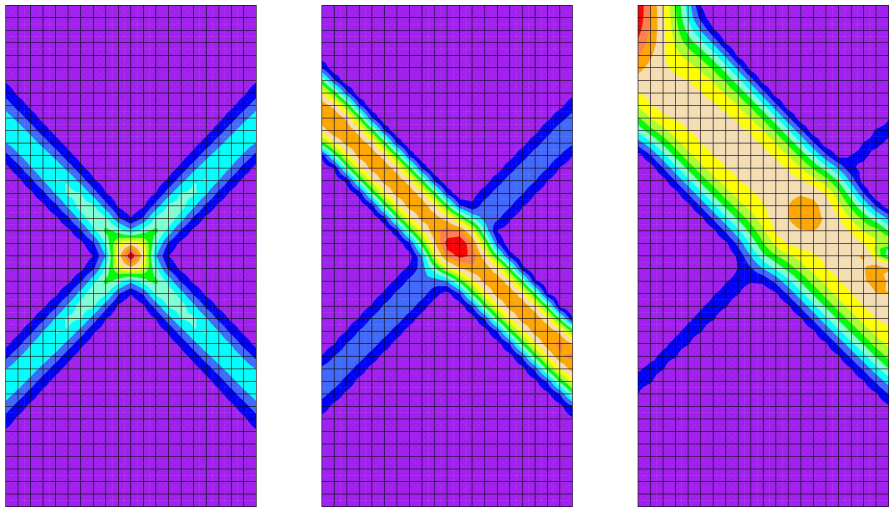

Fig. 8. Shear band evolution for the 10% imperfection located in the middle of the sample.

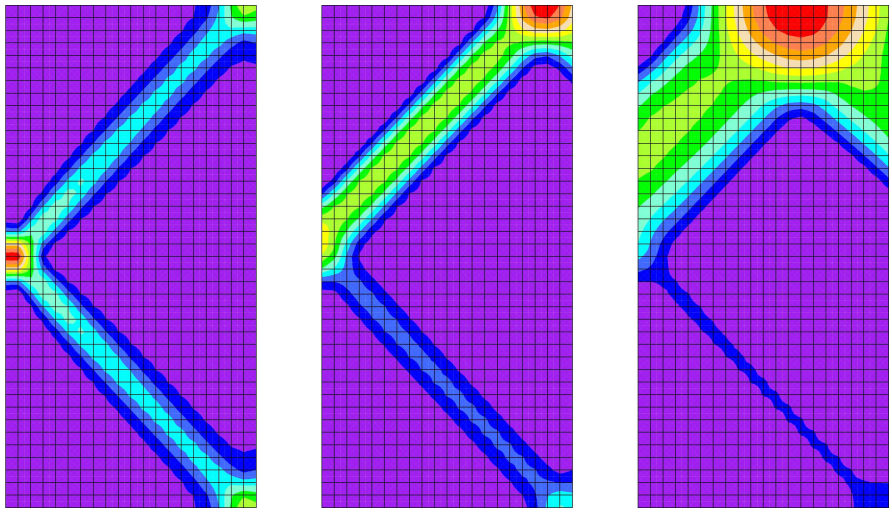

Fig. 9. Shear band evolution for the 10% imperfection located in the middle of the left edge of the sample.

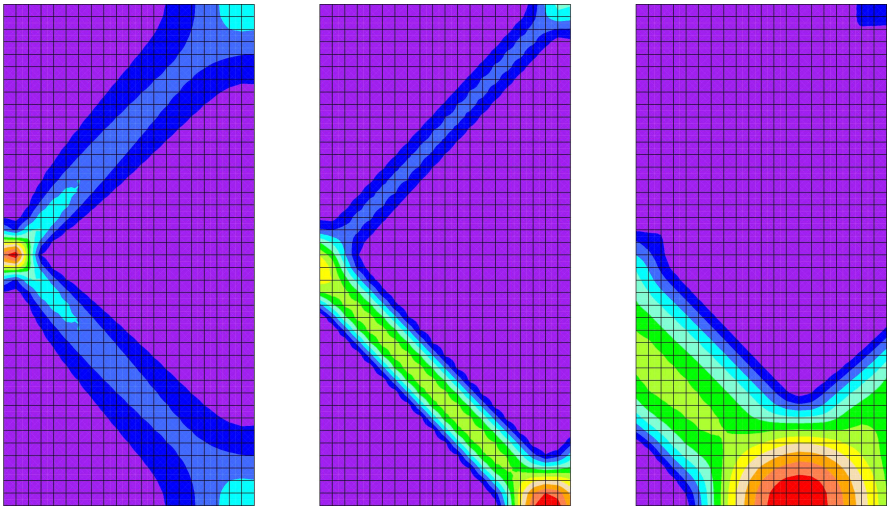

Fig. 10. Shear band evolution for the 1% imperfection located in the middle of the left edge of the sample.

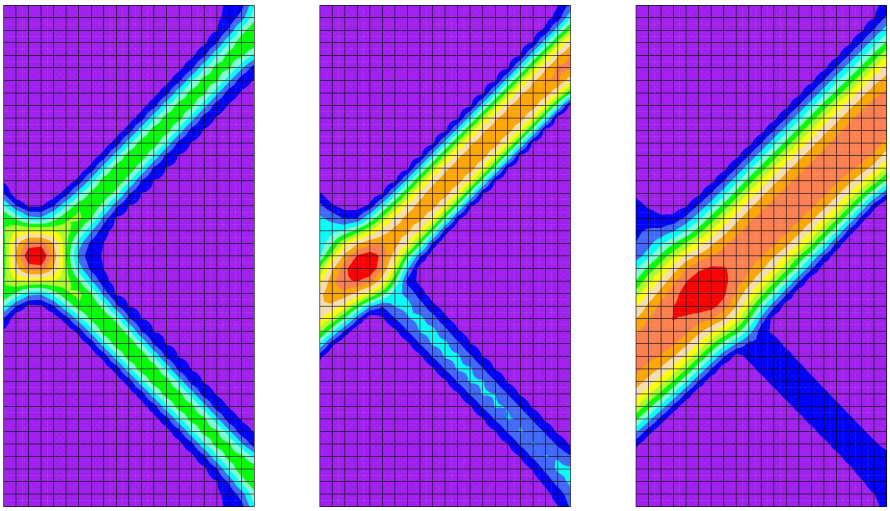

Fig. 11. Shear band evolution for the 10% sixteen-element imperfection located in the middle of the left edge of the sample.

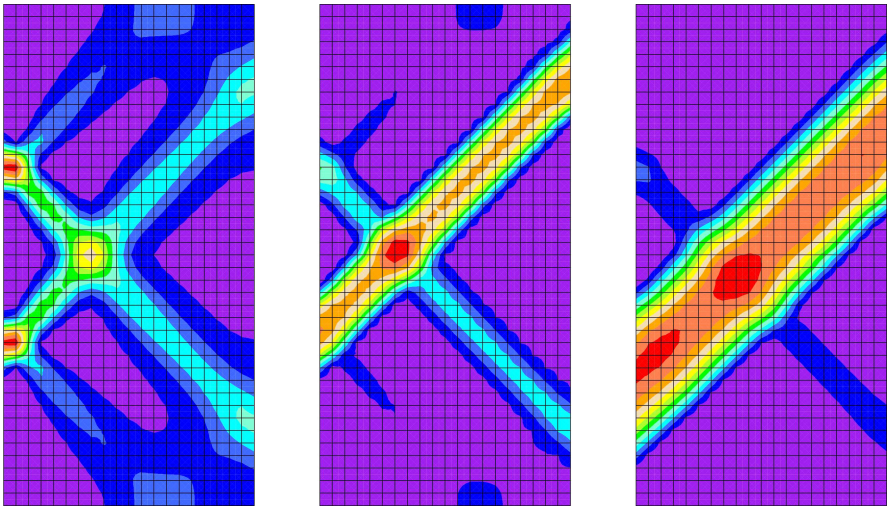

Fig. 12. Shear band evolution for two 10% imperfections located on the left edge of the sample.

tensor are shown for different stages of the loading process (for advanced plastic deformation $J_2{}^{\epsilon}$ represents quite closely the equivalent plastic strain). The shear band evolution is observed in all the cases. First a crossed pattern of bands is formed, then one of them remains active, because this is energetically preferable. Finally, as the critical state is approached, the band width increases. Unlike in gradient plasticity with a constant internal length parameter, standard (e.g., HMH) yield function and linear softening, in Cam-clay gradient plasticity the shear band width grows since softening is nonlinear. A uniaxial approximation of the relation between the gradient scaling coefficient g and the internal length scale l is $g = -hl^2$, where h is the evolving softening modulus, in this case the derivative of p_c with respect to $\Delta\Lambda$. The width of the shear band is governed by l and for the dilatant flow the derivative decreases, hence l apparently grows. To reduce this effect, the gradient factor g would have to be made a (decreasing) function of a plastic strain measure. This would physically mean a reduction of nonlocality as the critical state is approached which is not unrealistic and should be examined in the future research.

In the simulation presented in Fig. 10 the 1% smaller value of the initial preconsolidation pressure is assigned to the small area of the specimen to initiate the shear band formation. The shear band pattern is then qualitatively similar to the one obtained for 10% imperfection, shown in Fig. 9 but it is reflected with respect to the horizontal symmetry axis. Moreover, for the 10% imperfection assigned to a larger area (case D) the predicted shear band evolution is similar to case A, but its position is reflected with respect to the vertical symmetry axis. Finally, in Fig. 12 the results obtained for two imperfections are shown and the ones for advanced plastic process are similar to those obtained for the other cases.

It is concluded that the influence of the imperfection size and intensity on the evolution of the shear band width is negligible, since it is governed by l and h. On the other hand, it is observed that different positions and orientations of the shear band can be triggered in the simulation, so the solution of the problem is not unique although the alternative solutions are similar and physically sound.

7. Application – cut slope stability

As a practical application and a test of the developed two-phase model the stability of a cut slope is examined. The problem of pore pressure evolution combined with the gradient-enhancement of plasticity model is considered. The side length of a square specimen of soil is 10 m. The specimen is loaded by a rigid footing which extends over 7 m along the left part of the top surface. The drainage of the pore fluid ($p_f = 0$) is only allowed through the remaining part of the upper surface of the specimen. For points at the bottom edge of the sample the vertical displacement is prevented and at the right boundary of the specimen the horizontal displacement is not allowed. The configuration, loading and boundary conditions for the displacement and pore pressure fields are shown in Fig. 13.

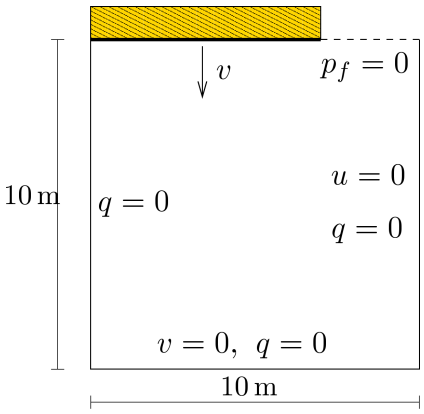

Fig. 13. Cut slope stability problem: geometry, natural and essential boundary conditions.

Note that for this configuration no imperfections are needed to trigger localization. The plastic multiplier is constrained in such a way that the normal and mixed derivatives $\Lambda_{,n}$ and $\Lambda_{,\xi\eta}$ are equal to zero on the whole circumference. To load the sample the vertical displacement of the rigid footing is prescribed. In fact, since the infinite stiffness of the footing has been assumed, it cannot rotate (although it can slide along the top edge) and thus equal vertical displacements of the upper nodes of the sample are prescribed. Due to the expected softening behaviour the loading is imposed under displacement control. The model is discretized with two- and three-field finite elements. Three densities of finite element mesh are considered: 10×10, 20×20 and 40×40.

Material data adopted in computations are as follows:

$\nu = 0.2$, $\kappa = 0.013$, $e_0 = 1.0$,

$p_c = 640.0$ kPa, $\lambda = 0.032$, $M = 1.1$,

$\gamma_f = 10$ kN/m^3, $K_f = 3.0e03$ kPa,

$k = 1.0 \times 10^{-4}$ m/day, $g = 1.0e05$ kN^2/m^2.

7.1. Cut slope stability – local Cam-clay simulation

To show the effectiveness of the applied gradient enhancement the results obtained for local and regularized models are discussed. For the local version of the modified Cam-clay model (two-field element) gradient scaling factor g is assumed to be equal to zero. The results of computations are presented in Figs. 14–17. The diagrams of reaction force versus vertical displacement for three different meshes are shown in Fig. 14. At the stage of the process when localization occurs the presented curves split and further do not coincide. In Fig. 15 the deformed meshes and in Fig. 16 the vertical strain distributions for the final state of calculations are plotted. The presented deformation patterns show that for each mesh strains localize in the narrowest possible area. The pore pressure distributions that do not exhibit localization are depicted in Fig. 17. However, it should be noted that the pore pressure distribution can be different for various values of the permeability coefficient, cf. [56].

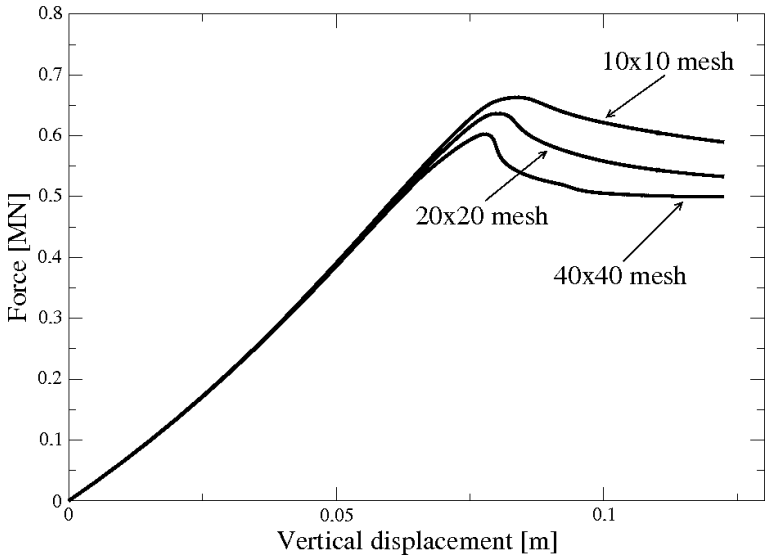

Fig. 14. Load-deformation curves for local Cam-clay model ($g = 0$).

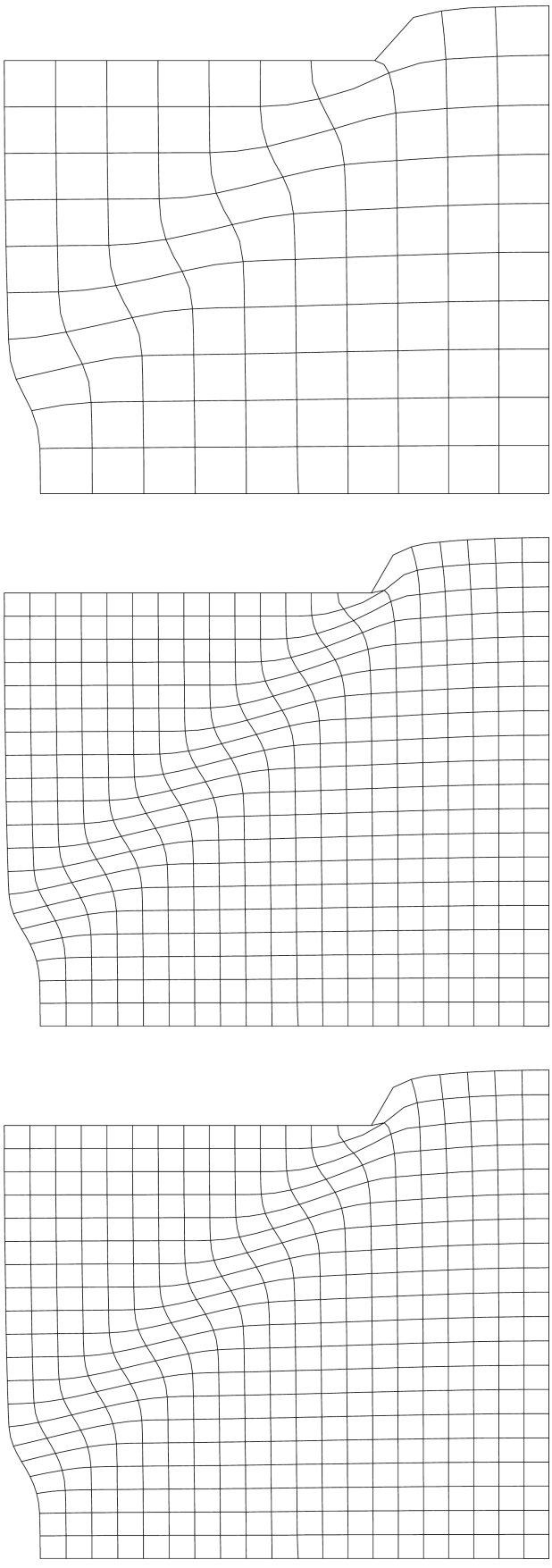

Fig. 15. Deformed meshes for local model.

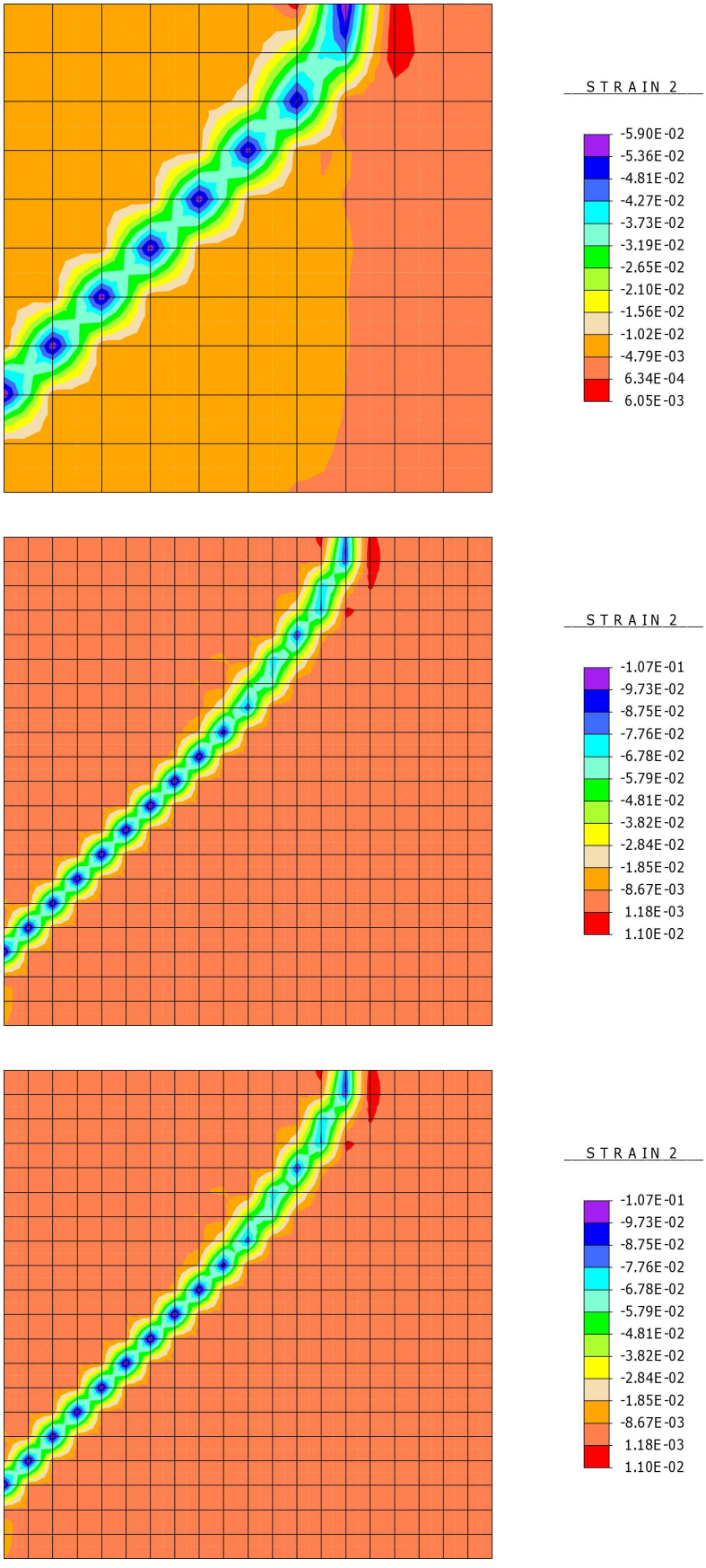

Fig. 16. Vertical strain distribution for local model.

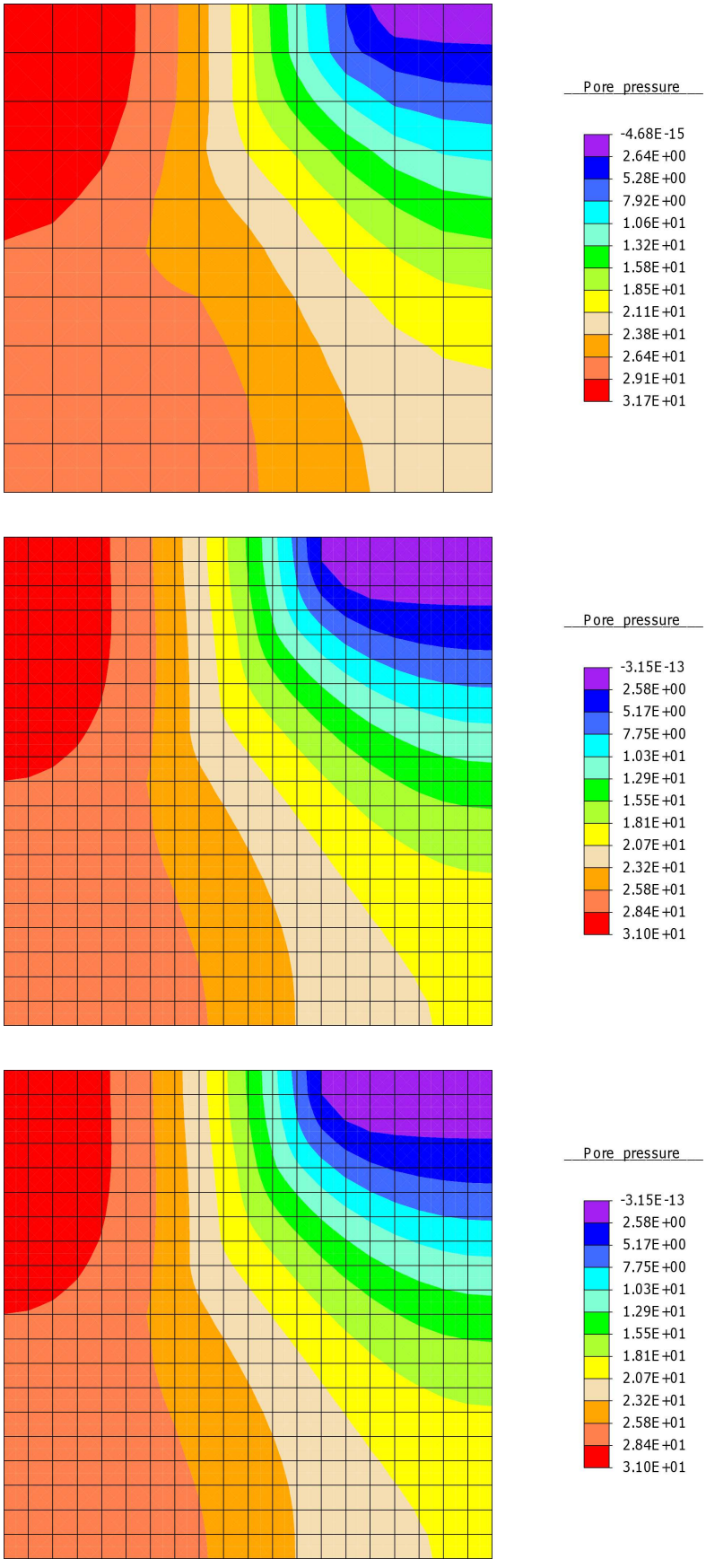

Fig. 17. Pore pressure distribution for local model.

7.2. Cut slope stability – regularized two-phase medium

Further results have been obtained for the gradient enhanced model (three-field element). As can be seen in Fig. 18 the results for the coarse mesh are not accurate enough due to a standard discretization error. However, the diagrams for the medium and the fine meshes almost coincide with each other. In Fig. 19 the deformed meshes and in Fig. 20 the vertical strain distributions are presented. This time the width of the shear band, which for the gradient model is in a relationship with the internal length introduced by the gradient scaling factor g, is similar for each of the three considered discretizations. The pore pressure distributions depicted in Fig. 21 do not depend on the mesh density and do not exhibit localization. Summarizing, the results for the gradient enhanced model are free from pathological discretization sensitivity. As shown in [56], for the two-phase Cam-clay model the pore pressure distribution depends on the permeability coefficient, but the shear band width does not.

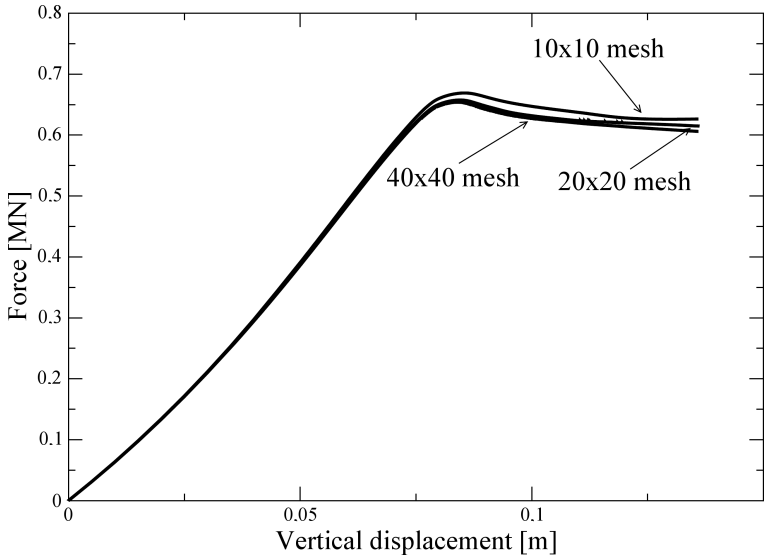

Fig. 18. Load-deformation curves for gradient-enhanced Cam-clay model $g = 1.0e05$ kN^2/m^2.

8. Final remarks

In this paper, the numerical simulations of strain localization in one- and two-phase geomaterials have been addressed. The influence of imperfections on shear band formation in the biaxial compression test of drained soil sample and the problem of slope stability have been presented.

In order to avoid the ill-posedness of the governing equations and to stabilize the numerical response in the presence of material softening the enhanced continuum theory has been applied. The gradient enhancement to the employed Cam-clay plasticity model has been introduced due to its universality and relatively convenient numerical implementation. Three and two-field finite elements implemented in FEAP package have been used in numerical simulations.

The examination of the influence of imperfections on shear band formation shows that, in static simulations, the role of imperfections is limited to the initiation of strain localization. When the pre-peak deformation is uniform (as in the biaxial compression test), imperfections trigger the localization process and determine the initial position of deformation bands. The size of imperfection area and intensity have no significant influence on the final shear band position. The location of imperfection affects the initial deformation pattern, i.e. the arrangement of shear bands. Further in the loading process the deformation with just one shear band is predominant. Its width is related to

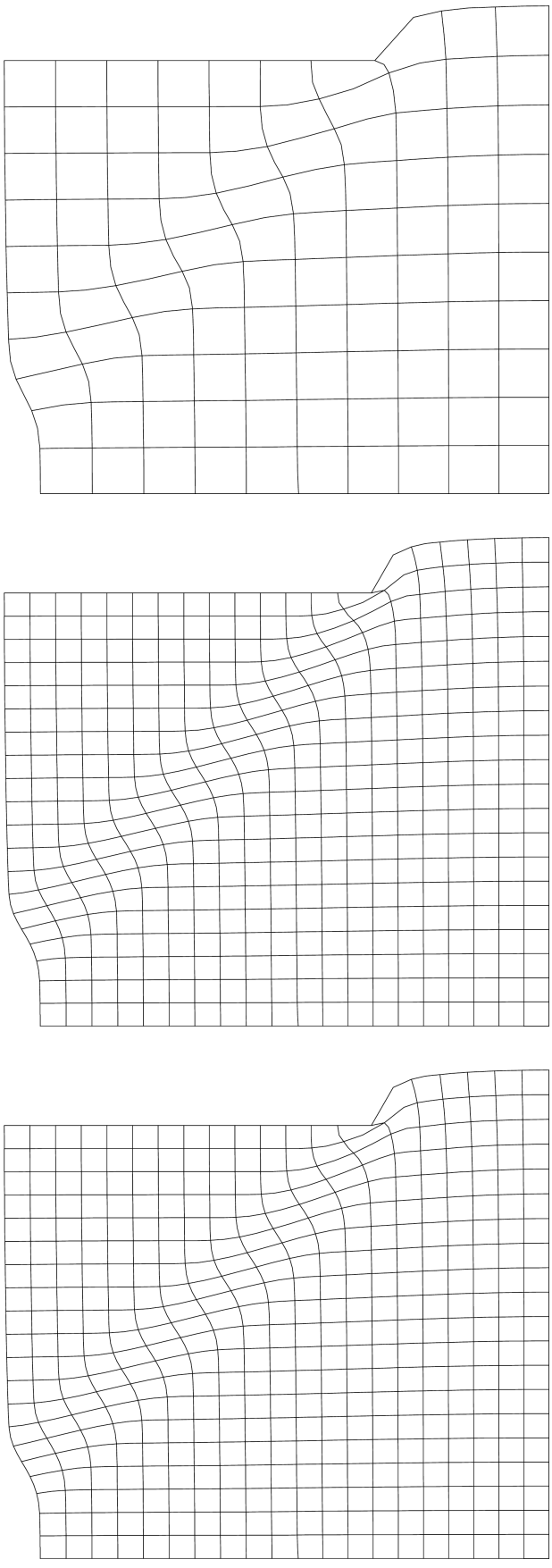

Fig. 19. Deformed meshes for gradient-enhanced Cam-clay model.

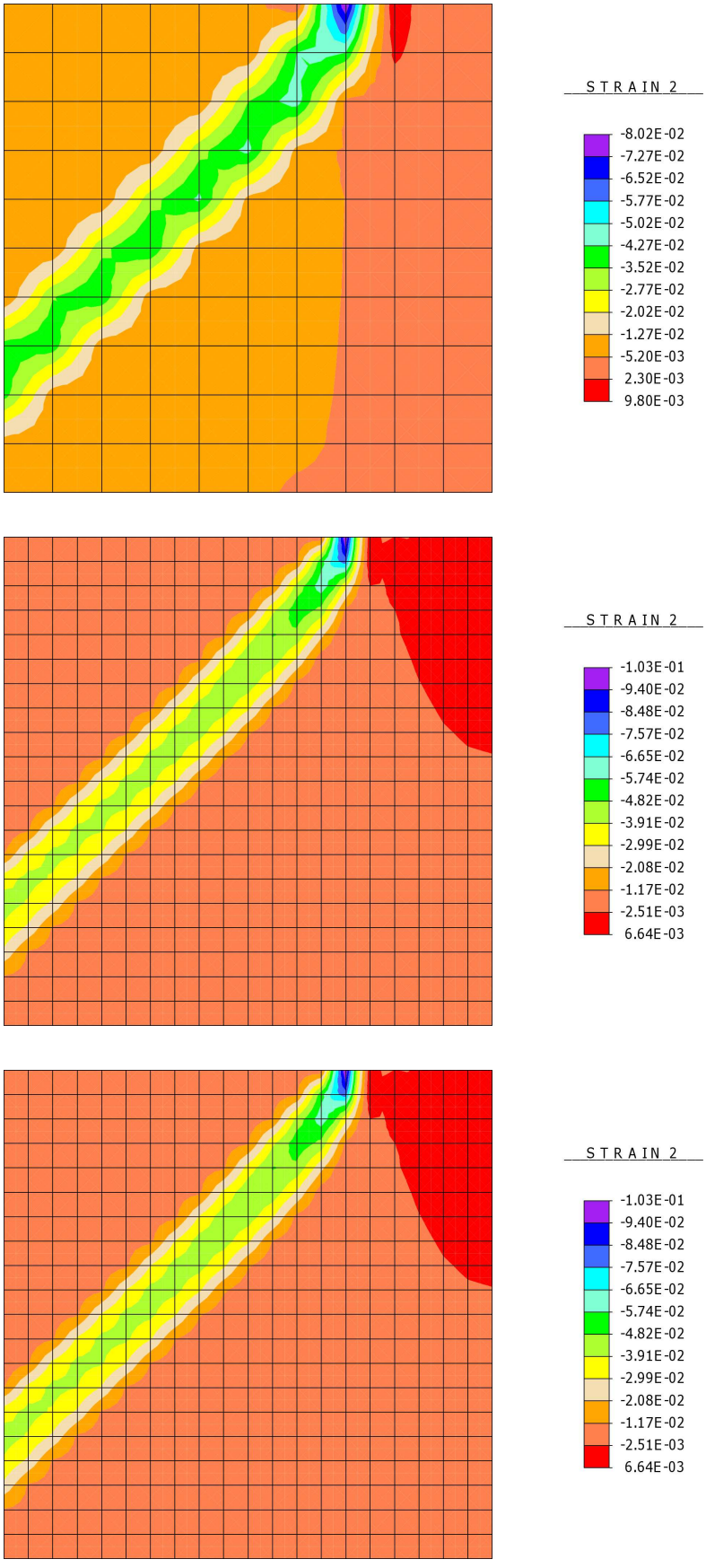

Fig. 20. Vertical strain distribution for gradient-enhanced Cam-clay model.

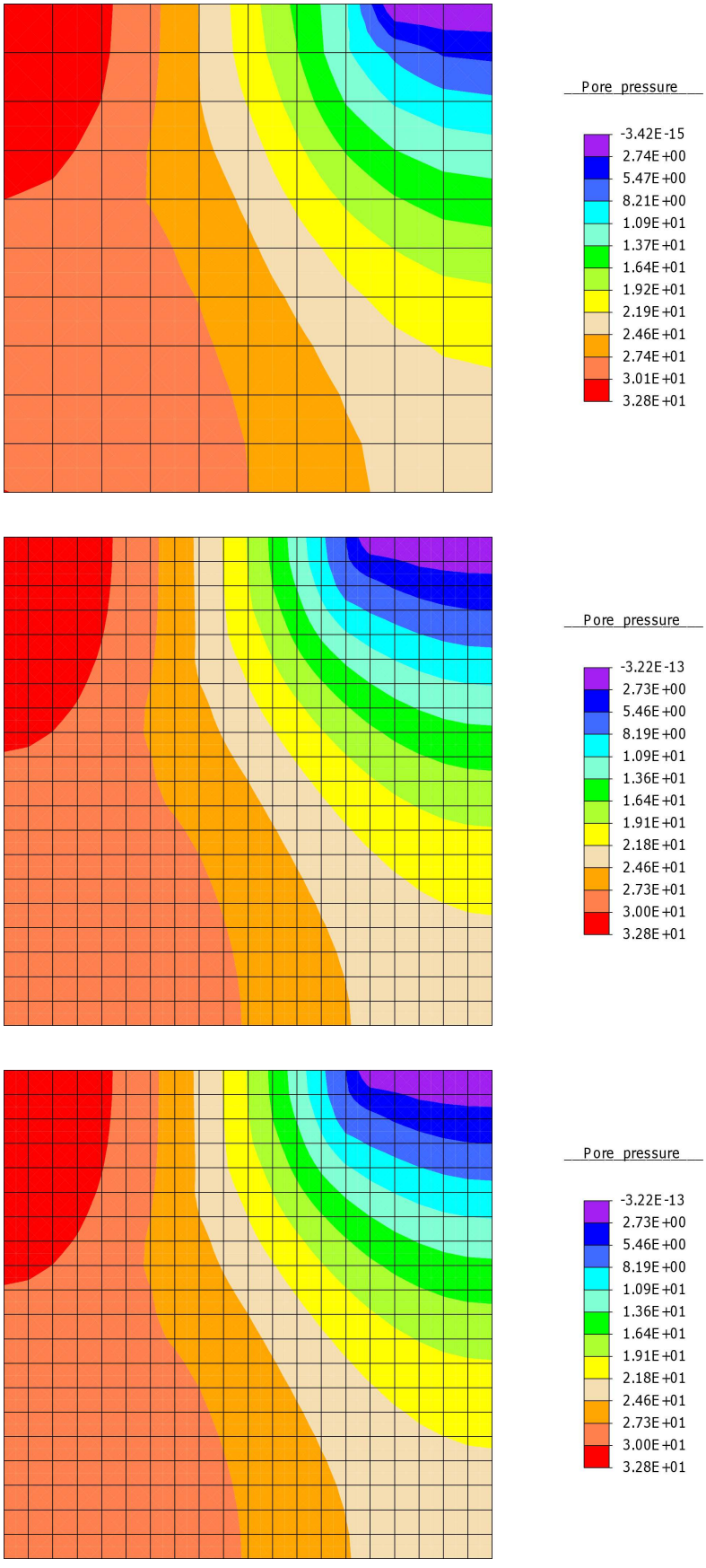

Fig. 21. Pore pressure distribution for gradient-enhanced Cam-clay model.

the internal length parameter and does not depend on area of imperfection. In the employed model the Laplacian influence scaling factor g is assumed to be constant, but the material hardening modulus evolves, hence the band width is observed to increase.

The analysis of steep slope stability problem with local Cam-clay model yield mesh-dependent distribution of strains while the gradient-enhanced version of the model provides discretization-independent solution.

The obtained results show that the gradient enhancement of Cam-clay model assures the well-posedness of BVP and eliminates the spurious mesh-sensitivity of discrete, numerical solutions by introduction of the internal length scale.

Acknowledgment

The author is grateful to Professor Jerzy Pamin for his helpful remarks and discussions during the preparation of this paper.

References

[1] E.C. Aifantis. Gradient material mechanics: perspectives and prospects. *Acta Mechanica*, **225**: 999–1012, 2014.
[2] H. Askes, A.S.J. Suiker, L.J. Sluys. A classification of higher-order strain-gradient models – linear analysis. *Archive of Applied Mechanics*, **72**(2-3): 171–188, 2002.
[3] I. Babuška, J.M. Melenk. The partition of unity method. *Int. J. Numer. Meth. Eng.*, **40**(4): 727–758, 1997.
[4] Z.P. Bažant, G. Pijaudier-Cabot. Nonlocal continuum damage, localization instability and convergence. *ASME J. Appl. Mech.*, **55**: 287–293, 1988.
[5] A. Benallal, J.-J. Marigo. Bifurcation and stability issues in gradient theories with softening. *Modelling and Simulation in Materials Science and Engineering*, **15**(1): 283–295, 2007.
[6] J. Bobiński. *Implementation and application examples of nonlinear concrete models with nonlocal softening*. Ph.D. dissertation, Gdańsk University of Technology, Gdańsk, 2006. (in Polish).
[7] R. Borja. Cam-Clay plasticity. Part V: A mathematical framework for three-phase deformation and strain localization analyses of partially saturated porous media. *Comput. Methods Appl. Mech. Eng.*, **193**: 5301–5338, 2004.
[8] R.I. Borja, X. Song, W. Wu. Critical state plasticity. Part VII: Triggering a shear band in variably saturated porous media. *Comput. Methods Appl. Mech. Eng.*, **261–262**: 66–82, 2013.
[9] R. de Borst. Simulation of strain localisation: A reappraisal of the Cosserat continuum. *Eng. Comput.*, **8**: 317–332, 1991.
[10] R. de Borst, M.-A. Abellan. Dispersion and internal length scales in strain-softening two-phase media. In G. Meschke et al. [Ed.], *Proc. EURO-C 2006 Int. Conf. Computational Modelling of Concrete Structures*, pp. 549–556, Taylor & Francis, London/Leiden, 2006.
[11] R. de Borst, H.-B. Mühlhaus. Gradient-dependent plasticity: formulation and algorithmic aspects. *Int. J. Numer. Meth. Eng.*, **35**: 521–539, 1992.
[12] R. de Borst, J. Pamin. Some novel developments in finite element procedures for gradient-dependent plasticity. *Int. J. Numer. Meth. Eng.*, **39**: 2477–2505, 1996.
[13] R. de Borst, L.J. Sluys, H.-B. Mühlhaus, J. Pamin. Fundamental issues in finite element analyses of localization of deformation. *Eng. Comput.*, **10**: 99–121, 1993.
[14] R. de Borst, E. van der Giessen, editors. *Material Instabilities in Solids*, Chichester, 1998. IUTAM, John Wiley & Sons.
[15] R.A.B. Engelen, M.G.D. Geers, F.P.T. Baaijens. Nonlocal implicit gradient-enhanced elasto-plasticity for the modelling of softening behaviour. *Int. J. Plasticity*, **19**(4): 403–433, 2003.
[16] S. Forest, E. Lorentz. Localization phenomena and regularization methods. In J. Besson [Ed.], *Local approach to fracture*, pp. 311–370. Les Presses de l'École des Mines, Paris, 2004.
[17] T.-P. Fries, T. Belytschko. The extended/generalized finite element method: an overview of the method and its applications. *Int. J. Numer. Meth. Eng.*, **84**(3): 253–304, 2010.
[18] A. Gajo, D. Bigoni, D. Muir Wood. Multiple shear band development and related instabilities in granular materials. *Journal of the Mechanics and Physics of Solids*, **52**: 2683–2724, 2004.
[19] M.G.D. Geers. *Experimental analysis and computational modelling of damage and fracture*. Ph.D. dissertation, Eindhoven University of Technology, Eindhoven, 1997.
[20] A. Gens, D.M. Potts. Critical state models in computational geomechanics. *Eng. Comput.*, **5**: 178–197, 1988.

[21] A. Glema. Analysis of wave nature in plastic strain localization in solids. Technical Report Monograph 379, Poznań University of Technology, Poznań, 2004. (in Polish).
[22] A. Glema, T. Łodygowski. On importance of imperfections in plastic strain localization problems in materials under impact loading. *Arch. Mech.*, **54**(5–6): 411–423, 2002.
[23] P. Grassl, M. Jirásek. Plastic model with non-local damage applied to concrete. *Int. J. Num. Anal. Meth. Geomech.*, **30**: 71–90, 2006.
[24] A. Groen. *Three-dimensional elasto-plastic analysis of soils*. Ph.D. dissertation, Delft University of Technology, Delft, 1997.
[25] M. Gryczmański. State of the art in modelling of soil behaviour at small strains. *Architecture Civil Engineering Environment*, **2**(1): 61–80, 2009.
[26] R. Hill. A general theory of uniqueness and stability in elastic-plastic solids. *J. Mech. Phys. Solids*, **6**: 236–249, 1958.
[27] T.J.R. Hughes. *The Finite Element Method.: linear static and dynamic analysis*. Prentice-Hall, New Jersey, 1987.
[28] M. Jirásek. Nonlocal models for damage and fracture: comparison of approaches. *Int. J. Solids Struct.*, **35**(31–32): 4133–4145, 1998.
[29] E. Kuhl, E. Ramm, R. de Borst. An anisotropic gradient damage model for quasi-brittle materials. *Comput. Methods Appl. Mech. Eng.*, **183**(1–2): 87–103, 2000.
[30] T. Liebe, P. Steinmann. Theory and numerics of a thermodynamically consistent framework for geometrically linear gradient plasticity. *Int. J. Numer. Meth. Eng.*, **51**: 1437–1467, 2001.
[31] T. Liebe, P. Steinmann, A. Benallal. Theoretical and computational aspects of a thermodynamically consistent framework for geometrically linear gradient damage. *Comput. Methods Appl. Mech. Eng.*, **190**: 6555–6576, 2001.
[32] A. Scarpas, X. Liu, J. Blaauwendraad. Numerical modelling of nonlinear response of soil. Part 2: strain localization investigation on sand. *Int. J. Solids Struct.*, **42**: 1883–1907, 2005.
[33] T. Łodygowski. Numerical solutions of initial boundary value problems for metals and soils. In Perzyna [46], pp. 392–468.
[34] G. Maier, T. Hueckel. Nonassociated and coupled flow rules of elastoplasticity for rock-like materials. *Int. J. Rock Mech. Min. Sci. & Geomech. Abstr.*, **16**: 77–92, 1979.
[35] N. Moës, J. Dolbow, T. Belytschko. A finite element method for crack growth without remeshing. *Int. J. Numer. Meth. Eng.*, **46**(1): 131–150, 1999.
[36] Z. Mróz. On forms of constitutive laws for elastic-plastic solids. *Arch. Mech.*, **18**: 3–34, 1966.
[37] H.-B. Mühlhaus, E.C. Aifantis. A variational principle for gradient plasticity. *Int. J. Solids Struct.*, **28**: 845–857, 1991.
[38] H.-B. Mühlhaus, I. Vardoulakis. The thickness of shear bands in granular materials. *Geotechnique*, **37**: 271–283, 1987.
[39] M.K. Neilsen, H.L. Schreyer. Bifurcations in elastic-plastic materials. *Int. J. Solids Struct.*, 30: 521–544, 1993.
[40] M. Ortiz, Y. Leroy, A. Needleman. A finite element method for localized failure analysis. *Comput. Methods Appl. Mech. Eng.*, **61**: 189–214, 1987.
[41] M. Ortiz, A. Pandolfi. A variational Cam-clay theory of plasticity. *Comput. Methods Appl. Mech. Eng.*, **193**: 2645–2666, 2004.
[42] N.S. Ottosen, K. Runesson. Properties of discontinuous bifurcation solutions in elasto-plasticity. *Int. J. Solids Struct.*, **27**(4): 401–421, 1991.
[43] J. Pamin. *Gradient-dependent plasticity in numerical simulation of localization phenomena*. Ph.D. dissertation, Delft University of Technology, Delft, 1994.
[44] J. Pamin. Numerical models of localized deformations (in Polish). In Biliński W. and Piszczek K., editors, *Proc. XVII Conf. Computer Methods in Design and Analysis of Hydrostructures*, pp. 77–86 Cracow University of Technology, Drukarnia "GS", Cracow, 2005.
[45] R.H.J. Peerlings, R. de Borst, W.A.M. Brekelmans, J.H.P. de Vree. Gradient-enhanced damage for quasi-brittle materials. *Int. J. Numer. Meth. Eng.*, **39**: 3391–3403, 1996.
[46] P. Perzyna, editor. *Localization and fracture phenomena in inelastic solids*. CISM Course Lecture Notes No. 386, Springer-Verlag, Wien – New York, 1998.
[47] H. Petryk, editor. *Material instabilities in elastic and plastic solids*. CISM Course Lecture Notes No. 414, Springer-Verlag, Wien – New York, 2000.
[48] H.E. Read, G.A. Hegemier. Strain softening of rock, soil and concrete – a review article. *Mech. Mater.*, **3**: 271–294, 1984.
[49] S. Rolshoven. *Nonlocal plasticity models for localized failure*. Ph.D. dissertation, École Polytechnique Fédérale de Lausanne, Lausanne, 2003.
[50] K.H. Roscoe, J.B. Burland. On the generalized behaviour of 'wet' clay. In *Engineering Plasticity*, **48**: 535–609, Cambridge University Press, Cambridge, 1968.
[51] J.G. Rots. *Computational modeling of concrete fracture*. Ph.D. dissertation, Delft University of Technology, Delft, 1988.

[52] J.W. Rudnicki, J.R. Rice. Conditions for the localization of deformation in pressure-sensitive dilatant materials. *J. Mech. Phys. Solids*, **23**: 371–394, 1975.
[53] M.S.A. Siddiquee. *FEM simulations of deformation and failure of stiff geomaterials based on element test results*. Ph.D. dissertation, University of Tokyo, Tokyo, 1994.
[54] L.J. Sluys. *Wave propagation, localization and dispersion in softening solids*. Ph.D. dissertation, Delft University of Technology, Delft, 1992.
[55] A. Stankiewicz. *Numerical analysis of strain localization in one- and two-phase geomaterials*. Ph.D. dissertation, Cracow University of Technology, Cracow, 2007.
[56] A. Stankiewicz, J. Pamin. Finite element analysis of fluid influence on instabilities in two-phase Cam-clay plasticity model. *Computer Assisted Mechanics and Engineering Sciences*, **13**(4): 669–682, 2006.
[57] A. Stankiewicz, J. Pamin. Gradient-enhanced Cam-clay model in simulation of strain localization in soil. *Foundations of Civil and Environmental Engineering*, **7**: 293–318, 2006.
[58] T. Svedberg, K. Runesson. A thermodynamically consistent theory of gradient-regularized plasticity coupled to damage. *Int. J. Plasticity*, **13**(6–7): 669–696, 1997.
[59] J. Tejchman. Influence of a characteristic length on shear zone formation in hypoplasticity with different enhancements. *Computers and Geotechnics*, **31**(8): 595–611, 2004.
[60] J. Tejchman. Effect of fluctuation of current void ratio on the shear zone formation in granular bodies within micro-polar hypoplasticity. *Computers and Geotechnics*, **33**(1): 29–46, 2006.
[61] J. Tejchman, W. Wu. Numerical study on patterning of shear bands in a Cosserat continuum. *Acta Mechanica*, **99**(1–4): 61–74, 1993.
[62] A. Truty. On certain class of mixed and stabilized mixed finite element formulations for single and two-phase geomaterials. Technical Report Monograph 48, Cracow University of Technology, Cracow, 2002.
[63] I. Vardoulakis, E.C. Aifantis. Gradient dependent dilatancy and its implications in shear banding and liquefaction. *Ing.-Arch.*, **59**: 197–208, 1989.
[64] I. Vardoulakis, J. Sulem. *Bifurcation Analysis in Geomechanics*. Blackie Academic & Professional, London, 1995.
[65] G.N. Wells. *Discontinuous modelling of strain localisation and failure*. Ph.D. dissertation, Delft University of Technology, Delft, 2001.
[66] K.J. Willam, A. Dietsche. Fundamental aspects of strain-softening descriptions. In Z.P. Bažant [Ed.], *Fracture Mechanics of Concrete Structures*, pp. 227–238, FRAMCOS, Elsevier Applied Science, London and New York, 1992.
[67] K.J. Willam, G. Etse. Failure assessment of the extended Leon model for plain concrete. In N. Bićanić et al. [Ed.], *Proc. Second Int. Conf. Computer Aided Analysis and Design of Concrete Structures*, pp. 851–870, Pineridge Press, Swansea, 1990.
[68] K. J. Willam, T. Münz, G. Etse, and Ph. Menétrey. Failure conditions and localization in concrete. In H.A. Mang et al., editors, *Proc. EURO-C 1994 Int. Conf. Computer Modelling of Concrete Structures*, pp. 263–282, Pineridge Press, Swansea, 1994.
[69] A. Winnicki, C.J. Pearce, N. Bićanić. Viscoplastic Hoffman consistency model for concrete. *Comput. & Struct.*, **79**: 7–19, 2001.
[70] M. Wójcik, J. Tejchman. Modeling of shear localization during confined granular flow in silos within non-local hypoplasticity. *Powder Technology*, **192**(3): 298–310, 2009.
[71] H.W. Zhang, B.A. Schrefler. Particular aspects of internal length scales in strain localisation analysis of multiphase porous materials. *Comput. Methods Appl. Mech. Eng.*, **193**: 2867–2884, 2004.
[72] O.C. Zienkiewicz, A.H.C. Chan, M. Pastor, B.A. Schrefler, T. Shiomi. *Computational Geomechanics*. John Wiley & Sons, Chichester, 2000.